# Lysozyme crystal growth kinetics in microgravity

**Fermín Otálora,[a]* Juan Manuel García-Ruiz,[a] Luigi Carotenuto,[b] Dario Castagnolo,[b] María Luisa Novella[a] and Alexander A. Chernov[c]**

*[a]Laboratorio de Estudios Crystalográficos, IACT, Campus Fuentenueva (Fac. Ciencias), 18002 Granada Spain, [b]Mars Center S.C.A.R.L. Naples Italy, [c]Universities Space Research Association. NASA/Marshall Space Flight Center. Huntsville, AL USA. E-mail: otalora@ugr.es*

Mach-Zehnder interferometry is applied to quantitatively characterize growth of lysozyme crystals in microgravity. Experiments were performed by the Free Interface Diffusion technique into APCF FID reactors using large seeds. Tracking of the experiments using interferometry allowed to monitor the onset of supersaturation and the seed growth. A large and stable concentration depletion zone around the growing crystal developed, whose time evolution was analyzed. The interferograms were analyzed taking into account finite thickness of the cell by integrating the concentration over the straight lines through the optical path. It was concluded that there may be a quasi-steady state growth mode at the stage when the spacial concentration distribution did not change but its absolute value over all the cell was slowly diminishing. From this portion of the data, an estimate was made of the dimensionless parameter $\beta R/D$ where $\beta$ is the face kinetic coefficient, $R$ is the effective crystal size and $D$ is the lysozyme diffusivity in solution, as followed from the steady state model. For the assumed quasi steady state data portion, the parameter varies between 0.7 and 0.9 suggesting mixed diffusion-interface kinetic controlled growth.

## 1. Introduction

Crystal growth from supersaturated solutions proceeds by the incorporation of growth units (atoms, molecules or small aggregates) from the solution to the crystal surface. In the absence of stirring or other fast fluid motion, this incorporation produces a concentration depletion zone (CDZ) around the crystal. The size (comparable to the crystal size) and shape of the CDZ are controlled by the coupled transport of the crystallizing species *via* diffusion in solution to the growing surface and the processes allowing these species to be incorporated into the lattice. In the presence of fast fluid motion, i.e. natural or forced convection, a zone depleted in growth units in which mass transport is essentially diffusive is still present as the so called "boundary layer", but this layer is much narrower than the crystal size.

Here we study the coupling between bulk diffusion and incorporation at the crystal interface taking advantage of microgravity conditions and the lack of fast fluid motion. Evaluation of relative contributions of these two factors can allow to estimate the surface supersaturation and impurity composition both of which may influence the crystal quality. This knowledge is of fundamental significance for understanding microgravity assisted crystal growth, where the crystal quality may be improved because of better ordering due to slower growth (García Ruiz, 1999) and impurity filtering (McPherson *et al.*, 1999; Thomas *et al.*, 2000). Two requirements are needed to develop the concentration depletion zone, namely: a) to ensure diffusive mass transport (this is the role of microgravity) and b) to have the crystal growing in the diffusion controlled or mixed regime.

Studies of the two simultaneous processes, diffusive mass transport and surface attachment, detachment or reorganization, require *in-situ*, non-intrusive monitoring techniques. Apart from direct microscopic observation and measurement of growth rates, mainly three such techniques have been used: on one hand atomic force microscopy (AFM) and Michelson interferometry (MI) are used to investigate crystal surface kinetics and, on the other, Mach-Zehnder interferometry (MZI) and Michelson interferometry are used to study mass transport in the bulk solution. Other techniques such as ultraviolet light transmission microscopy (Kam *et al.*, 1978), microscope light scattering (Gorti *et al.*, 2001), Schlieren optics (Pusey *et al.*, 1988) or Moiré fringes (Hirano & Ogawa, 1981) have also been used occasionally for this kind of studies.

*In situ* AFM studies during macromolecular crystal growth (Durbin & Carlson, 1992; Durbin *et al.*, 1993; Konnert *et al.*, 1994; McPherson *et al.*, 1995; Land *et al.*, 1995; Kuznetsov *et al.*, 1996*a*; Land *et al.*, 1996; Li *et al.*, 1999; Malkin *et al.*, 1999; Kuznetsov *et al.*, 1999; Nakada *et al.*, 1999; Land & De Yoreo, 2000; Rong *et al.*, 2000; Wiechmann *et al.*, 2001; Kuznetsov *et al.*, 2001; Yau *et al.*, 2001; Malkin *et al.*, 2001) have shown the details of the surface morphology at the nanometer scale, including the growth mechanisms operating (screw dislocations, two dimensional nucleation...) and have provided quantitative information on key parameters such as the free energy of the step edge per unit step height $\alpha$ or the kinetic coefficient of elementary steps $\beta_s$, estimated to be $1.6 \times 10^{-3}$ cm/s for Canavalin (Land *et al.*, 1997; Land & De Yoreo, 2000), $3.2 \times 10^{-5}$ cm/s for Catalase (Malkin *et al.*, 1997) $(4–8) \times 10^{-4}$ cm/s for STMV (Land *et al.*, 1996) and $2.4 \times 10^{-4}$ cm/s for Thaumatin (Malkin *et al.*, 1996; Malkin *et al.*, 1999). The main problem of AFM in studying crystal growth kinetics is that the relative movement of the surface and the cantilever may influence mass transport rate and thus the supersaturation at the surface (Land *et al.*, 1996). Crystal growth kinetics of biological macromolecules has been also investigated by measuring the growth rate and surface morphology using Michelson Interferometry (MI) (Monaco & Rosenberger, 1993; Vekilov *et al.*, 1993; Vekilov, 1993; Kuznetsov *et al.*, 1995; Vekilov *et al.*, 1995; Kuznetsov *et al.*, 1996*b*; Vekilov & Rosenberger, 1996; Vekilov & Rosenberger, 1998), which has the advantage over AFM of being completely non-intrusive, although spatial resolution is worse despite of some efforts to improve it (Onuma *et al.*, 1993; Vekilov *et al.*, 1995). MI can, in principle, be used in diffusive set-ups such as microgravity crystal growth facilities (Maruyama *et al.*, 1998; Tsukamoto *et al.*, 1998), but in practice most growth kinetics experiments are performed under natural or forced convection (Vekilov & Rosenberger, 1998). Typical MI studies concentrate on detailed descriptions of the growth rate and on the average morphology of the growing face, in particular on the distribution and activity of hillocks around screw dislocation step sources. These studies also provide quantitative information on the $\beta_s$ kinetic coefficient. Values gathered from literature shows values of $9 \times 10^{-4}$ for Canavalin (Kuznetsov *et al.*, 1995) and $1.7 – 2.5 \times 10^{-4}$ for Lysozyme (Vekilov, 1993). These AFM and MI studies shows a three order of magnitude differences in free energy of the step edge per unit step height and kinetic coefficient between macromolecular and small molecule crystals (see for example Teng *et al.* (1998) and Rashkovich (1991) for data on $CaCO_3$ and KDP respectively). As the surface energy per molecular site is of the same order of magnitude in both systems (Chernov, 1997), a significantly higher entropic barrier must exist for macromolecular crystal growth (Chernov & Komatsu, 1995; Rosenberger *et al.*, 1996).

Mass transport in the bulk solution around the growing crystals has been investigated mostly using Mach-Zehnder Interferometry (MZI) (McPherson *et al.*, 1999; Sazaki *et al.*, 1996; Snell *et al.*, 1996; García-

  

Ruiz *et al.*, 1999; Otálora *et al.*, 2001) and Michelson Interferometry (MI) (Komatsu *et al.*, 1993; Miyashita *et al.*, 1994; Kurihara *et al.*, 1996; Hou *et al.*, 2001). MZI studies the concentration depletion zone around the growing crystal, the influence of the experimental setup on the global supersaturation environment, and the effect of crystal movement, residual acceleration and g-jitters on the stability of the CDZ, while MI studies usually concentrate on the local properties of the concentration gradient close to the crystal surface to estimate local supersaturation, solubility or diffusion coefficients.

These complementary approaches to crystal growth kinetics have been developed separately, AFM results being restricted to surface kinetics, MZI studies to bulk mass transport kinetics and MI being used for both types of studies but always in separate experiments. No results have been reported on the dynamic coupling of surface and bulk kinetics and no cross checking of the quantitative information from these two approaches is available, although facilities exist that allow the simultaneous recording of growth rate (by MI) and mass transport (by MZI) both in normal and reduced gravity (Tsukamoto *et al.*, 1998; Maruyama *et al.*, 1998). Since the bulk solution mass transport and surface kinetics are coupled, it is in principle possible to study the whole process looking at just one of them, provided that the needed conceptual tools exist to a) get quantitative information on the observed process and b) to make the right assumptions on the other (not observed) process. Studying surface kinetics by MI or AFM is perfectly suited for the first requirement, but the complex (non diffusive) dynamics of the bulk solution in both experimental set-ups poses problems for the second one. Therefore we decided to study the mass transport kinetics in the bulk solution by using a non-intrusive technique (MZI) for getting quantitative information on the kinetics of both coupled processes as a whole. With these objectives we developed the experimental techniques to get accurate quantitative information from interferometric data while using a well known kinetic model to consistently provide the link between both processes. Starting with MZI data on the concentration depletion zone around a lysozyme crystal growing in microgravity, these data were corrected and fit to a quasi-steady-state model for stagnant crystal growth from solution. A check was then performed on how the macroscopic properties of the mass transport in the bulk solution and the growth of the crystal surface are explained by the kinetic parameters obtained. This paper concentrates on macromolecular crystal growth in diffusive media with special implications for microgravity, but the experimental techniques and the concepts involved are of rather general applicability to crystal growth from solution.

## 2. Kinetic model

Some interesting models have been used to extract information on the surface kinetics from bulk solution mass transport data (Maruyama *et al.*, 1998; Kam *et al.*, 1978; Miyashita *et al.*, 1994). All these approaches depend on the accurate measurement of the concentration gradient at the crystal / solution interface, a quantity hard to obtain. In this work, a classical formulation (Chernov, 1984) is used to obtain information on key kinetic parameters. This quasi-steady-state formulation for stagnant crystal growth under diffusive mass transport predicts a concentration distribution around the crystal

$$C(r) = C_\infty - (C_\infty - C_0)\frac{\beta R/D}{1+\beta R/D}\frac{R}{r} \tag{1}$$

and a crystal growth rate of

$$V = \frac{\Omega\beta(C_\infty - C_0)}{1+\beta R/D} \tag{2}$$

where $r$ is the distance from the center of the crystal, $C_\infty = \lim_{r\to\infty} C(r,t)$ is the homogeneous bulk concentration far from the crystal, $C_0$ is the thermodynamic equilibrium concentration (concentration of the saturated solution), $R$ is the radius of the crystal (assumed to be spherical), $D$ is the diffusion coefficient of the growth units in the bulk solution, $\Omega$ is the volume of the growth unit and $\beta$ is the so called *kinetic coefficient of growth from solution*. $\beta$ and $\beta_s$ are different quantities related by $\beta = p\beta_s$ where $p$ is the hillock slope from the direction of the singular face. Concentration units (for $C_\infty$ and $C_0$) are number of growth units per unit volume. Equations (1) and (2) describe, within the order of magnitude, the coupled dynamic evolution of mass transport in the bulk and the incorporation of growth units to the crystal surface. The properties of these equations can be better understood by defining the dimensionless quantities

$$\tilde{r} \equiv \frac{r}{R},\ \tilde{C}(\tilde{r}) \equiv \frac{C(\tilde{r}) - C_\infty}{C_\infty - C_0},\ k \equiv \frac{\beta R}{D} \tag{3}$$

In terms of these dimensionless parameters, the concentration and the concentration gradient are respectively

$$\tilde{C}(\tilde{r}) = -\frac{k}{1+k}\frac{1}{\tilde{r}} \tag{4}$$

$$\frac{\partial\tilde{C}}{\partial\tilde{r}} = \frac{k}{1+k}\frac{1}{\tilde{r}^2} \tag{5}$$

the concentration and the gradient at the solution/crystal interface ($\tilde{r} = 1$) being

$$\left.\frac{\partial\tilde{C}}{\partial\tilde{r}}\right|_{int} = -\tilde{C}(1) = \frac{k}{1+k} \tag{6}$$

The form of equation 6 is shown in figure 1. Two limiting growth regimes and a smooth transition between them can be defined as a function of the ratio of surface incorporation rate to the bulk transport rate, the slower one being the rate controlling process. At $\beta R/D \ll 1$ (left part of plot), the CDZ vanishes ($C(r) \simeq C_\infty$ for any $r$ so that $\tilde{C} \simeq 0$), and the growth rate is determined completely by the surface kinetics and is independent of the crystal size, which increases linearly with time as $R \simeq \beta(C_\infty - C_0)\Omega t$. This is the so-called kinetic regime of growth. If $\beta R/D \gg 1$, (right part of plot) then the deepest possible gradient exists with $C(r) \simeq C_\infty - (C_\infty - C_0)R/r$, ($\tilde{C} \simeq -1/\tilde{r}$) and the crystal size grows as $R \simeq D\sqrt{2\Omega(C_\infty - C_0)t}$, completely limited by bulk diffusion and independent of the kinetics of surface processes. This is the diffusion controlled regime in which a CDZ of depth $C_\infty - C_0$ develops as $C(R) = C_0$. Between these two limiting regimes, the so-called "mixed regime" extends in which concentration, gradient and growth rate have intermediate values controlled by both mass transport and surface kinetics, neither of them being negligible. This means that the solution in contact with the crystal surface is not saturated, but supersaturated, the local supersaturation being larger for crystals growing closer to the kinetic regime and the gradients being larger for crystals growing closer to the diffusion controlled regime. The experimental confirmation of this fact (Miers, 1904) triggered the development of the classical diffusion/reaction kinetic models like the one used here.

During steady-state growth of the crystal at constant $\beta$ and $D$, $k$ changes with time (because $R$ does) so experiments does not proceed at a fixed point in the curve in figure 1. This means that the relative importance of each of the two processes and even the growth regime can change during the growth history of a single crystal.

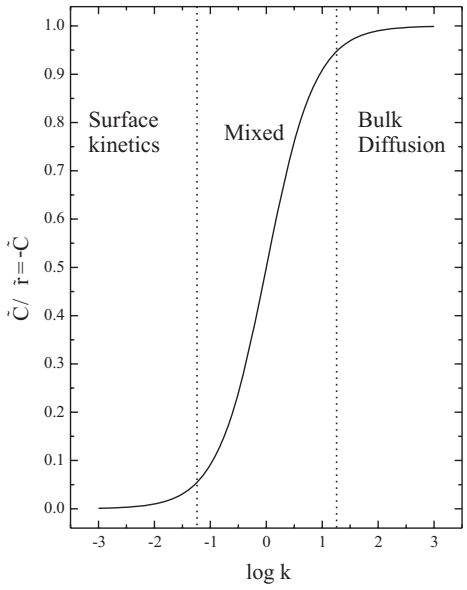


**Figure 1**
Concentration and gradient at the crystal surface as a function of $k \equiv \beta R/D$. Regions where crystal growth is controlled by surface kinetics or by diffusion are indicated. *k*-positions of vertical dotted lines separating these regions are arbitrarily selected for illustration purposes.

### 3. Experimental

Experiments were designed to quantitatively characterize the concentration depletion zone around a growing protein crystal. So a *non moving, single, large* crystal was grown in a cell where *diffusive mass transport was ensured*. This cell was observed by *in-situ Mach-Zehnder Interferometry* to record the crystal and the surrounding concentration distribution (expected to be a *large*, *unique* CDZ) *in time*.

Evidently, to have a CDZ stable enough in time, diffusive mass transport is required. Different approaches have been proposed for having experimental setups for crystal growth from solution under diffusive mass transport (gels, capillaries, microgravity) (Robert *et al.*, 1999). Among them, microgravity has the advantage over gels of being free of macromolecular interactions that could modify in unexpected ways the transport and surface kinetics. Microgravity allows for the about-pure diffusive transport in three-dimensions and the possibility of growing larger crystals than in capillaries (just because of growth cell size constraints). This is important as the crystal size is one of the parameters involved in the kinetic model. Microgravity experiments were performed in the Advanced Protein Crystallization Facility (APCF) (Bosch *et al.*, 1992) provided by ESA during the STS-95 mission of the NASA Space Shuttle. Free interface diffusion (FID) reactors were selected to avoid liquid/gas interfaces that could lead to disturbing Marangoni convection as in the case of vapor diffusion techniques (Savino & Monti, 1996; Chayen *et al.*, 1997). These reactors have a 15 mm long precipitating agent reservoir separated from the protein chamber ($5 \times 5$ mm cross section, 8 mm long) by a turnable block having a built-in channel (12 mm long) initially filled with buffer solution (figure 2). By turning this block, the precipitating agent and protein solution can be set in contact once in orbit.

The CDZ around a moving crystal in microgravity has been shown to be distorted by crystal movements (Otálora *et al.*, 2001). To avoid these potential distortions, a macro-seeding technique was used. The crystals required for our experiments were grown from a fixed macro-seed glued to the wall of the protein chamber (see figure 2). Large seed crystals (up to 16 $mm^3$ in volume) can be grown in high concentration silica gels (García-Ruiz *et al.*, 1998). This growth technique is known to produce "reinforced" crystals that can be easily handled and even glued to rigid substrates. After performing vibration tests with the reactors containing these seeds mounted into the APCF flight model, we decided to use seeds grown in 5% w/v tetramethoxysilane silica gels and to fix them directly on the reactor wall using cyanocrylate adhesive.

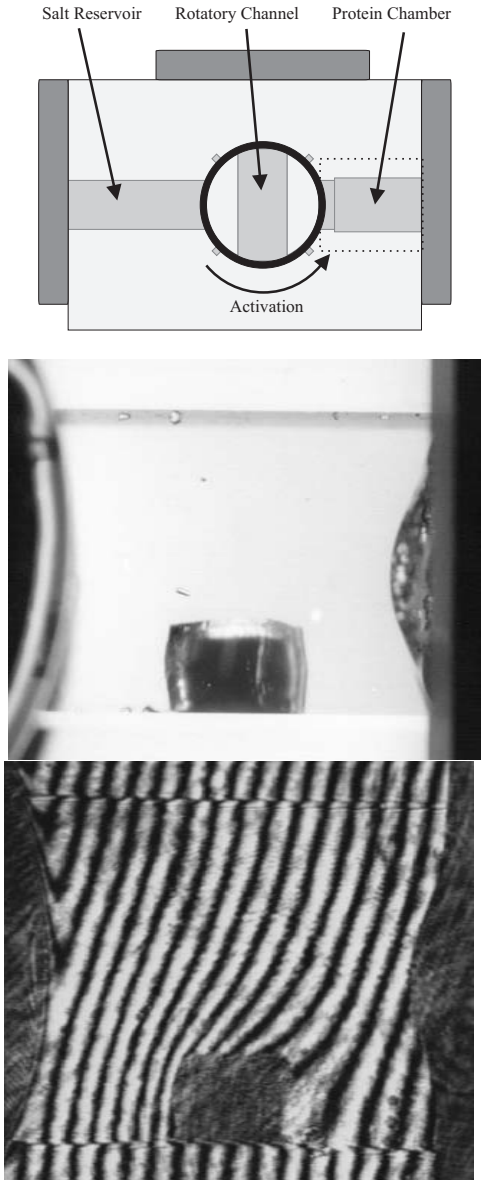


**Figure 2**
Top: Schematic view of the APCF FID reactor used in the experiment. The salt reservoir, rotatory channel (in the unactivated position) and the protein chamber are shown. The curved arrow indicates the activation mechanism by rotation of the channel. The dotted rectangle depicts the area shown in the images below corresponding to the protein chamber as seen by low magnification optical microscopy (middle) and interferometry (bottom). NaCl enters the protein chamber from the left side through the rotatory channel after activation

The crystal had to be single and large in order to produce a large enough CDZ for quantification of the concentration gradient. Concentration depletion zones have been already observed around small

non isolated crystals using interferometry (Boggon *et al.*, 1998), but no information other than just the existence of the CDZ can be derived from these observations. Therefore, the initial conditions were selected on the basis of keeping the growth chamber solution within the metastable zone of the phase diagram, allowing the growth of the seed but avoiding further nucleation that would spoil the interferometry data. During the whole experiment, temperature was kept at $20 \pm 0.3^{\circ}$ C by the APCF temperature control system (Lautenschlager, 2002). The equilibration pathways through the solubility diagram were carefully studied using both computer simulation and on-ground test experiments. 89.5 mg/ml solutions of lysozyme (Seikagaku E98301) containing 1.2% w/v of sodium chloride (Sigma analytical grade) were used in the protein chamber. The rotatory channel was filled with a gelled (0.5% w/v agarose) 1.3% w/v solution of sodium chloride and the salt reservoir with an ungelled 3.25% w/v solution of sodium chloride. The three solutions were buffered to pH 4.5 in 0.5 M sodium acetate buffer. Using these initial conditions, undisturbed growth of the seed was achieved during the first 100 hours of the experiment, followed by the homogeneous nucleation of a number of very elongated crystals (aspect ratio $L_c/L_a \simeq 3$, $L_i$ being the length along the crystallographic axis $i$), which indicate a very low supersaturation (Durbin & Feher, 1986).

The APCF Mach-Zehnder interferometer (Snell *et al.*, 1996) powered by a 850 nm laser diode was used to collect interferograms from the reactor in microgravity following a pre-programmed data acquisition sequence. A pseudo phase shifting method was used to improve the accuracy of the phase images. This method consists of imposing a small angle between the wavefronts of the test and reference beams so the "white" image (before activation of the experiment) already has a number of parallel fringes. The measurement of fringe deviation in a small refractive index gradient is then more accurate than the measurement of small changes in intensity (gray level) (Robinson & Reid, 1993; Breuckmann, 1993). The evaluation of interferograms was done in the following way: every interferogram was transformed to a phase image by triangulation and interpolation (Akima, 1978) from a dense set of points lying on interference fringes of the interferogram; the proper refractive index was assigned to each fringe by fringe counting at a point far from the seed crystal. Real phase values were obtained by subtracting the reference phase field (the one computed from the reference "white" interferogram before activation) from each phase map. Phase difference maps were transformed to concentration difference maps by using refractive index *versus* concentration calibration curves previously obtained in our laboratory by refractometry and extrapolated using the Cauchy equation. The concentration maps obtained were corrected for geometrical distortions using procedures explained in the "Results" section.

Figure 2 shows the experimental setup. The picture on the middle was taken after the space mission; the seed crystal is clearly seen glued to the wall of the protein chamber. The dark central part of the crystal corresponds to the initial seed, the lighter parts around it to the crystal volume grown while in microgravity. Color differences are due to the inclusion of silica gel in the crystal lattice of the seed (García-Ruiz *et al.*, 1998). The interferometry image (figure 2, bottom) was taken aboard the Shuttle during the mission. The overall field of roughly vertical fringes was initially imposed to implement the pseudo-phase-shift technique. The CDZ is seen as a distortion of this fringe pattern: the initially vertical fringes are bent down by a distance proportional to the decrease in protein concentration at this point (Komatsu *et al.*, 1993; Miyashita *et al.*, 1994). The width of the protein chamber is 5 mm.

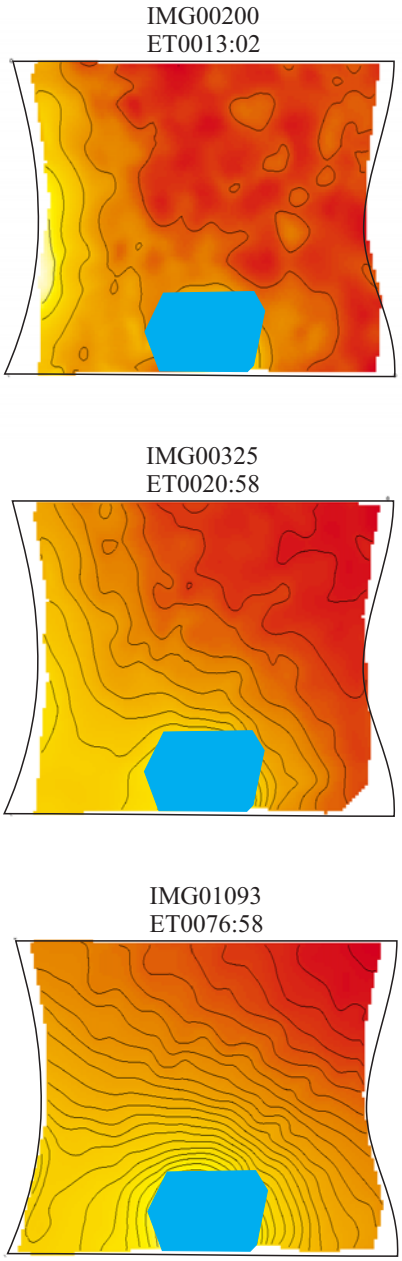


**Figure 3**
Maps of refractive index reconstructed from the interferograms collected during the experiment. Image code and APCF Elapsed Time are indicated on top of each map. Contour lines correspond to $2\pi/5$ differences in phase, corresponding to 0.312 mg/ml differences in protein concentration. The limit of the protein chamber is indicated by the continuous line boundary.

## 4. Results and discussions

Figure 3 shows some selected maps of the refractive index inside the protein chamber during the experiment as computed from the interferograms. The development of two different gradients is observed: the CDZ as a "radial" gradient around the growing crystal and a second gradient "parallel" to the direction of mass transport between the rotatory channel and the protein chamber. Right after the activation of

the experiment, diffusive mass transport between the different chambers of the reactor starts, giving rise to the "parallel" gradient. Protein starts leaving the protein chamber toward the rotatory channel while salt starts diffusing in the opposite direction. As the protein concentration difference between the protein chamber and the channel is large (89.5 mg/ml, corresponding to Δn=0.00976) as compared to the salt concentration difference (1 mg/ml, corresponding to Δn=0.00018), the net effect observed is a decrease in the refractive index at the left side of the protein chamber as shown in the first map. The seed overgrowth at this time is almost inexistent, so no concentration depletion zone is observed around the crystal. Eight hours later (second map) the entry of salt from the salt reservoir increases the supersaturation in the protein chamber and the seed starts growing. This causes the depletion of protein concentration around the seed that gives rise to the CDZ. This "radial" concentration gradient around the crystal is combined with the previously mentioned "parallel" gradient due to the transport of salt and protein between the protein chamber and the rotatory channel. The relative importance of these two gradients changes with time: the depth of CDZ around the crystal increases with time as the seed grows while the "parallel" gradient is progressively relaxed. Consequently, as the experiment evolves, the net concentration distribution shows a deep "radial" gradient around the crystal slightly distorted by a shallower "parallel" gradient (third map). Eventually, both gradients relax as equilibrium is approached.

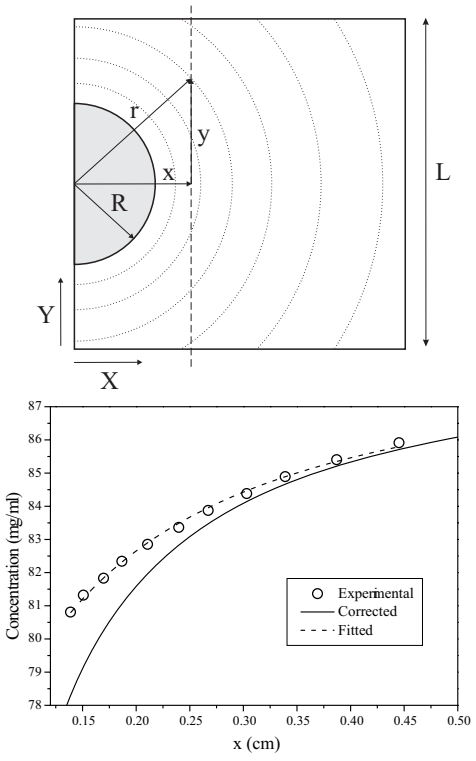


**Figure 4**
Sketch of the top view of a growth reactor showing the geometry of the three-dimensional integration of refractive index in wide cells (top). $C(r)$ is the concentration at all points at the same distance $r$ from the center of the crystal (dotted lines). $R$ is the crystal size. $L$ is the optical path through the chamber. Integration occurs along the dashed line (in the direction of the laser beam). Example of fitting and geometrical correction used in this work (bottom). Apparent concentration values $C(x)$ obtained from the interferograms are shown as open circles. Equation 8 is used to fit these data (dashed line). Using the fitted parameters, corrected $C(r)$ concentration values are computed from equation 1 (solid line).

Raw experimental data (i.e. refractive index maps) cannot be used directly to calculate concentration values by fit to equation (1) as the values computed from the interferograms represent the integration of refractive index along the optical path (figure 4, top). From figure 4 (top), it is evident that

$$C(x) = \int_{-L/2}^{L/2} C(r)dy \qquad (7)$$

Inserting equation (1) for the concentration and substituting $r = \sqrt{x^2 + y^2}$, equation 7 can be solved to

$$C(x) = C_\infty - (C_\infty - C_0)\frac{\beta R/D}{1+\beta R/D} R \log \frac{\sqrt{x^2 + (L/2)^2} + L/2}{\sqrt{x^2 + (L/2)^2} - L/2} \qquad (8)$$

Equation 8 was used as the fit model for the apparent concentration gradients computed from the experimental interferograms. Parameters obtained from this fit were used to compute the real gradients using equation (1). Figure 4 (bottom) shows the stages and the effect of the correction. The corrected concentrations do approach the measured ones for large $r$ while the correction is significant for the low $r$'s, i.e. in the proximity of the crystal surface. This makes very unreliable the evaluation of local supersaturation at the crystal surface if no correction is applied (Onuma *et al.*, 1993). In these fits, only two parameters were adjusted, $C_\infty$ and $\beta/D$. $C_\infty$ can not be estimated from experimental conditions because its physical meaning is undefined after the concentration decrease at the wall opposite to the seed becomes non negligible. Obviously $\beta$ and $D$ can not be adjusted separately as they always appear together as a quotient in the fitting model; $C_0$ values were computed from a lysozyme solubility curve obtained from data gathered from the literature (see Otálora & García-Ruiz (1997) for more details) and $R$ values were measured from the images acquired during the experiment. Including these values (particularly $C_0$) as free parameters for fitting increases the parameter dependency making the fitting unstable and rendering impossible in practice to estimate $\beta/D$.

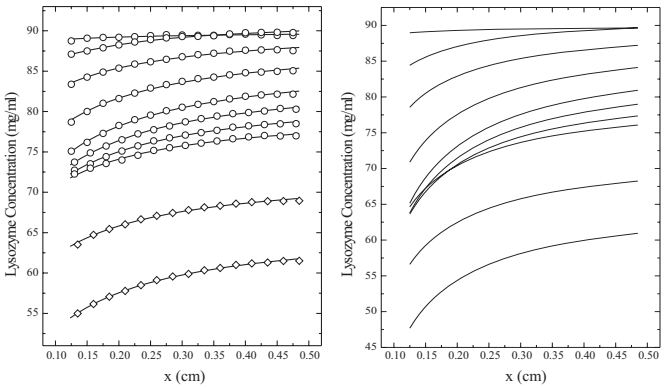


**Figure 5**
Apparent (left) and corrected (right) concentration profiles. Open circles represent experimental data, lines in the plot at left are the apparent concentration gradients (equation 8) fitted to experimental data. Data is shown for interferograms collected at APCF Elapsed Time 13:02, 24:59, 33:11, 41:59, 52:43, 64:49, 76:58, 91:16, 110:19, and 130:39 (hh:mm, from top to bottom respectively). The plot at right shows the actual concentration gradients for the same times after correction of the three-dimensional integration effect.

Figure 5 (left) shows the apparent concentration values extracted from a series of concentration maps computed from interferograms collected during the growth of the crystal in microgravity along with the

corresponding fits to equation 8. Concentration gradients were taken along the perpendicular to the 110 face of the crystal, i.e. along vertical lines through the center of the seed crystal in figure 2. This orientation was chosen to avoid any possible effect of the "parallel" gradients due to salt and protein moving in and out of the protein chamber. Figure 5 (right) shows the same profiles after correction for three dimensional integration effects. The development of the concentration depletion zone from the almost homogeneous initial concentration is clearly seen in figure 5 (first and second curves from top to bottom). At some time between 12 and 20 hours elapsed time, the CDZ starts interacting with the wall of the reactor (third and fourth curves). This produces a decrease of the protein concentration at the reactor wall. After 40 hours, the concentration at the crystal surface and thus the growth rate changes slowly, as does the concentration in the bulk solution in the cell. This is the period closest to a quasi steady state while such state is never achieved in reality in this experiment. After the crystal was growing in this quasi steady state mode for almost 40 hours, nucleation occurs in the whole solution homogeneously. As a result, the bulk concentration starts decreasing rapidly. The effect of this nucleation is shown by the last two curves in figure 5. As this nucleation heavily influences the concentration distribution within the whole depletion zone (see section 3.), in what follows, the concentrations measured after this nucleation are not shown.

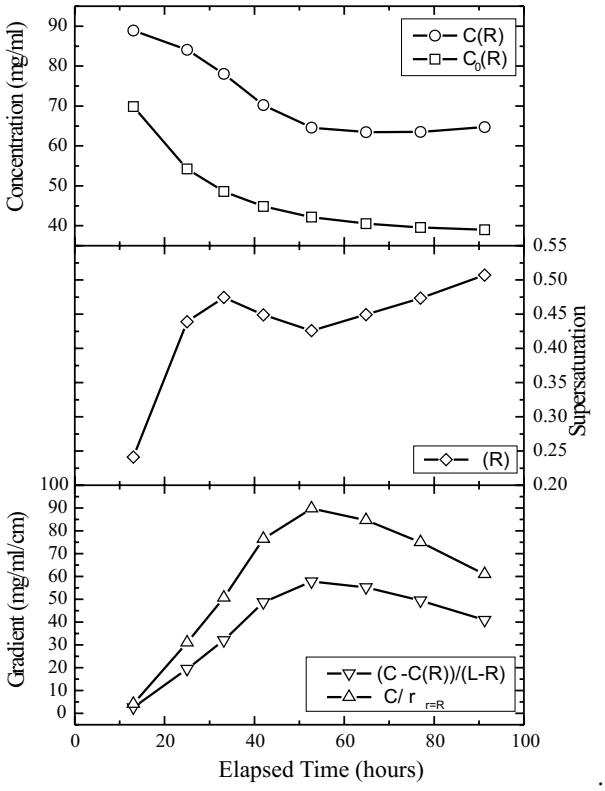


**Figure 6**
Time evolution of the protein concentration at the crystal surface ($C(R)$), solubility ($C_0$), supersaturation ($\sigma$), overall concentration gradient ($(C_\infty - C(R))/(L-R)$) and local concentration gradient ($\partial C/\partial r|_{r=R}$)

Figure 6 shows the time evolution of local protein concentration, solubility, supersaturation and concentration gradient at the crystal surface along with the overall concentration gradient into the protein chamber. These data shows for the first time the complex setting and evolution of CDZ around a crystal growing in microgravity and the effects of these dynamics on key quantities as the local protein concentration and concentration gradient.

The decreasing solubility at the crystal surface ($C_0(R)$) is due to the increasing salt concentration in the protein chamber. Its time evolution depicts the relaxation of the salt gradient along the three chambers of the reactor (a total of 35 mm) during the experiment. To reduce this time dependency of solubility by having smaller salt gradients within the system, some salt was initially included in the protein chamber (see section 3.), but obviously some gradient must be present to ensure crystal growth at a measurable rate at constant temperature. After an initial period (0–32 hours) of fast supersaturation increase due to the initially large increase of salt concentration (and the subsequent fast reduction in solubility), the supersaturation reaches a maximum when $\partial C_0(R)/\partial t = \partial C(R)/\partial t$ (0.7 mg/ml/hour) and then starts to decrease slowly to a minimum 52 hours after activation. During this period, the CDZ is developed via spreading the protein diffusion front from the growing crystal interface into the cell depth (the crystal was initially in contact with the saturated solution before activation). After this time, the crystal grows from $R$ =1.21 mm to $R$ =1.28 mm close to steady state, with slower decreases in the local and overall gradients affected by finite size of the cell (the CDZ is large enough to interact with the wall of the protein reservoir at 3.9 mm from the crystal surface). During this period, the supersaturation increases slowly due to the continuous increase of salt concentration. At the same time, the protein concentration at the crystal surface is almost constant because the minor decreases in solubility are compensated by the slower supply of protein molecules due to finite size effects. To put it shortly, there is rather complex interplay between salt and protein non-steady state diffusion which determine evolution of both the concentrations and the supersaturation. Because of this complex evolution, the protein concentration at the interface ($C(R)$) cannot be fitted to a quasi-steady state equation ($C(R) = a + b/(cR)$) (Chernov, 1984) over the whole experimental time, deviations being concentrated in the far from steady state periods.

The time averaged measured supersaturation at the crystal surface $\sigma = \ln C(R)/C_0 = \Delta\mu/kT$ during the growth of the crystal is 0.47. This is low as compared with the supersaturations reported in previous publications. However, the comparison must be done carefully as the values provided here correspond to local supersaturation *at the crystal surface* while *overall supersaturation* is commonly reported elsewhere. In this supersaturation range, crystal is expected to growth layerwise by screw dislocations (Vekilov & Rosenberger, 1996; Kuznetsov *et al.*, 1996*a*) and the growth rate is expected to be lowered due to the effect of impurities (Chernov & Malkin, 1988). The effect of impurities cannot be checked in our experiment and could lead to an underestimation of $\beta R/D$ coefficients, but this effect (if present) must be small due to the high purity of the reactants used in the experiment. Unfortunately, we do not have the growth rate versus supersaturation dependence for the material used in these experiments to plug into more rigorous analysis.

Data on concentrations, supersaturations and concentration gradients were obtained from local values of the fitted function (that for the calculation of these values was used just as an extrapolating function) so they are almost unaffected by the presence of periods of non steady state growth, provided the fit is good. In contrast, the fitted $\beta/D$ values depend on the global shape of the fitted function so they are affected by these deviations, the point being to understand how these deviations affect the estimation of $\beta$. Therefore what follows may be considered as a qualitative attempt to extract orders of magnitude for the parameters involved in the process.

Figure 7 shows the evolution of the apparent $k \equiv \beta R/D$ dimension-

less coefficient obtained from fitting. If all assumption relevant for the linear steady state model would held, this curve should be parallel to the *R versus* time curve (see figure 8) as $\beta/D$ is supposed to be constant. The relative change of the parameter $\beta R/D$ during the time of the steady state growth should be equal to that of R (around 6 %), an order of magnitude smaller than that shown in figure 7.

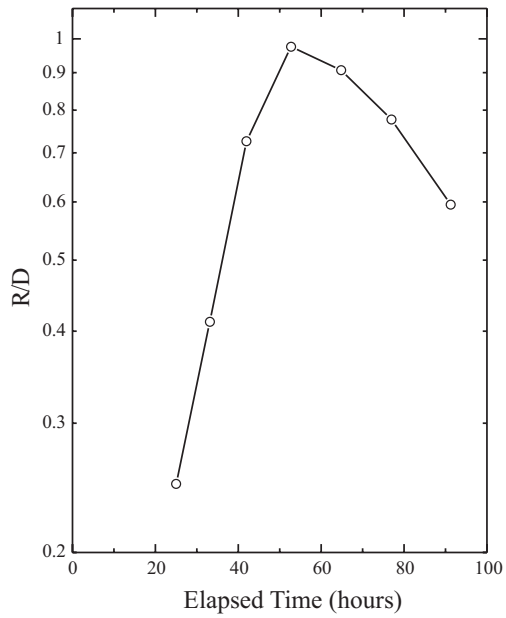


**Figure 7**
Time evolution of $\beta R/D$ during the experiment. Each data point corresponds to a curve in figure 5.

Strictly speaking, $D$ is a changing quantity depending on the protein and salt concentration (Albright *et al.*, 1999); $\beta$ can also change as a function of supersaturation, in case of a non-linear dependence of the growth rate on supersaturation. However, these changes can not explain by themselves the large changes observed. As in the case of protein concentration gradients, the two main effects contributing to this behavior are the initial development of the CDZ and the finite size of the growth reactor. Both effects produce an underestimation of $\beta/D$ when fitting, as the gradients predicted by the model are larger than those experimentally observed. Therefore, the best estimation of the true $\beta R/D$ coefficient is the value at the maximum, where the deviation from the ideal behavior is minimal. Within these limitations, the value of the $\beta R/D$ coefficient can be estimated from these results to be 0.9, corresponding to a mixed growth regime. Assuming a diffusion constant $D \simeq 1 \times 10^{-6}\text{cm}^2/s$ for lysozyme (Muschol & Rosenberger, 1996), this would correspond to $\beta \simeq 8.0 \times 10^{-6}$ cm/s about an order of magnitude of previously reported values (Vekilov, 1993). This difference could be related to the uncertainties in the interpretation of the present data and to the different experimental approach used: In previous works, $\beta$ was estimated as the slope of the plot of $V$ (growth rate) *versus* $\sigma$ (supersaturation); even in experiments performed under forced convection, a boundary layer exists close to the crystal surface where protein concentration decreases toward the crystal. As a consequence, for any crystal growth experiment in the mixed regime, the slope of the curve $V = f(\ln(C_\infty/C_0))$ used for the estimation of $\beta$ in the absence of data on the local concentration at the crystal surface is smaller than the slope of the curve $V = f(\ln(C(R)/C_0))$ that would be the $\beta$ estimation best suited for comparison with our results. With the $\beta R/D$ value obtained, the linear model presented in section 2. predicts (equations 3 and 4) a constant concentration at the crystal surface $C(R) = 57$ mg/ml in good agreement with the measured 63 mg/ml value close to steady state (for the period between 52 and 92 hours).

Obviously, the apparent $\beta R/D$ values obtained from the fits and plotted in figure 7, make no sense when deviations from the steady state are large (at the beginning and the end of the experiment) and for this reason, they are not taken into account for the estimation of the $\beta$ kinetic coefficient. Nevertheless, at the local scale, right at the crystal surface, the protein concentration and the gradient of protein concentration as well as the solubility and supersaturation are correctly predicted by these values so the data plotted in figure 6 are correct for the whole time range shown.

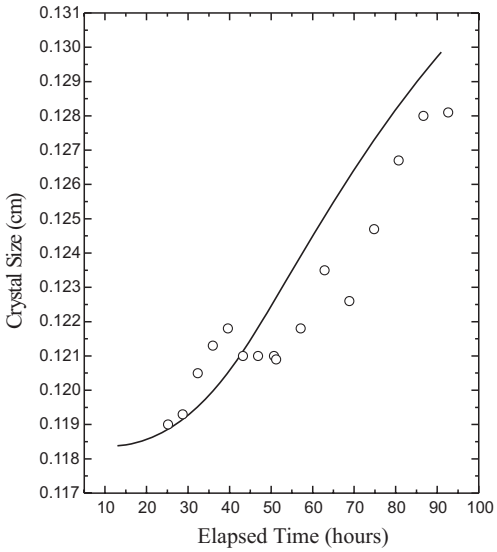


**Figure 8**
Variation of crystal size during the growth experiment. Open circles correspond to experimental data (as in figure 6 bottom). The solid line is the size computed by numerically integrating equation 2 using $C_\infty$ and $\beta/D$ values interpolated from the values obtained by fitting.

The theoretical crystal size expected from the kinetic model can be computed by numerically integrating equation 2. To this end, look-up tables were computed by interpolating the time dependent values of $C_\infty$ and apparent $\beta/D$ obtained from the fits. $\Omega$ was set to 20.6 $\text{nm}^3$ (a sphere with radius 1.7 nm (Durbin & Feher, 1986)). Concentration-dependent $D$ values were used as reported by Muschol & Rosenberger (1996). Figure 8 shows the comparison of the values computed in this way (solid line) and the values experimentally measured. Computed and experimental values are in good agreement, which shows the self-consistency of the values obtained. The solid curve shows an initial part of increasing growth rate corresponding to the initial development of the concentration depletion zone followed by a period of almost constant growth rate and, finally a slow decrease of the growth rate due to protein exhaustion owing to the finite cell size effects already discussed. The overall shape of the growth curve is therefore controlled by both the steady-state and the non-steady-state features of the experiment, which explains why the crystal size evolution is well predicted by integrating the time dependent growth rate, but cannot be fit over the whole experiment duration to the one predicted by the linear model. From 45 hours on, experimental data is always below the theoretical value (yet parallel to it). This occurs after a period of close to zero growth rate starting at $t \simeq 42$ hours, corresponding to the maximum protein concentration gradient but also to the release of the Spartan

satellite during the STS-95 mission. Whether this transient change in the growth rate is due to the transport dynamics or to a period of large g-jitters cannot be concluded from our data, but similar effects due to large g-jitters at this time have been reported for other experiments aboard the same mission (García Ruiz *et al.*, 2001).

## 5. Conclusions

The simultaneous, coupled processes of bulk mass transport and surface incorporation of growth units can (and should) be studied as a whole. To this end, Mach-Zehnder interferometry measurements of the dynamics of the concentration depletion zone around a growing crystal are shown to be a useful tool. Raw interferometric data must be corrected for detailed data analysis if the width of the growth cell is not negligible in the direction of the optical path. This correction is non-trivial when the growth cell is large enough to allow interactions of the CDZ with the reactor walls.

The growth of lysozyme crystals in diffusive media proceeds in the mixed regime due to the development of a large concentration depletion zone that evolves toward quasi steady state if the CDZ is stable enough i.e. if the crystal is not moving and the distance between growing crystals is larger than the diameter of the CDZ. During the dynamic evolution of the CDZ, concentration gradients are controlled by both bulk mass transport (of both the protein and the precipitant) and by surface kinetics. Furthermore, the initial setup of the CDZ and finite-size effects that modify the concentration gradients also influence the relative importance of both diffusion and surface incorporation processes as shown by the changes observed in the apparent kinetic coefficient $k \equiv \beta R/D$. The strong influence of the non-steady state diffusion of the protein and the salt allow the steady state model to provide only very preliminary results on the value of $\beta$. With these reservations in mind, the more reliable value for the kinetic coefficient provided by the steady-state approximation is $\beta R/D = 0.9$, corresponding to $\beta \simeq 8.0 \times 10^{-6}$ cm/sec. As the presence of non-steady-state periods is related to the activation mechanism and the geometry of the growth cell, they will affect any crystal growth experiment performed using this kind of facilities, and must be taken into account when studying the results of experiments using microgravity facilities for the growth history of the crystal can not be reproduced or even understood on the basis of fix or slightly changing kinetic coefficients. This means that design of the future experiments should include mechanisms allowing to minimize the non-steady state processes, e.g. by initial stirring, and to have in possession the interface kinetic controlled growth rate as a function of supersaturation. The finite size of the crystallization cell should also be taken into account in the full scale modeling of the process.

The benefits of crystal growth in diffusive media, in particular in microgravity conditions, can only be obtained if the crystal grows by addition of growth units supplied at a slow rate by diffusive mass transport through a stable CDZ filtering the potentially disturbing protein or impurity concentration changes at the crystal surface. Therefore, for microgravity experiments, the definition of experimental conditions ensuring the development of a stable CDZ is a requirement as important as having a quiet diffusive environment. It should be noted that this requirement extends not only to the "Diffusion Controlled" regime, but also to the "Mixed" regime in which a CDZ also develops. Nevertheless, one must keep in mind that the noise filtering efficiency of the CDZ is larger for deeper CDZ's. On the other hand, even when diffusive transport is ensured, no warranty exists that the crystal will grow in the "diffusion controlled" or "mixed" regimes: the growth regime in which the crystal will grow is a function of the ratio between diffusion transport and surface attachment kinetics.

We acknowledge financial support from CICYT (project ESP98-1347), European Union (project BIO4-CT98-0086) and the *Consejo Superior de Investigaciones Científicas* (CSIC). This work has been possible thanks to an APCF flight opportunity provided and supported by the European Space Agency. We would like to thank the APCF team of Astrium for their help with APCF reactors and vibration tests during the preparation of experiments.

## References

Akima, H. (1978). *ACM Trans. Math. Soft.* **4**(2), 148–159.

Albright, J. G., Annunziata, O., Miller, D. G., Paduano, L. & Pearlstein, A. J. (1999). *J. Am. Chem. Soc.* **121**, 3256–3266.

Boggon, T. J., Chayen, N., Snell, E. H., Dong, J., Lautenschlager, P., Potthast, L., Siddons, D. P., Stojanoff, V., Gordon, E., Thompson, A. W., Zagalsky, P. F., Bi, R.-C. & Helliwell, J. R. (1998). *Phil Trans. R. Soc. Lond. A*, **356**, 1045–1061.

Bosch, R., Lautenschlager, P., Potthast, L. & Stapelmann, J. (1992). *J. Crystal Growth*, **122**, 310–316.

Breuckmann, B. (1993). *Bildverarbeitung und optische Metechnik in der industriellen Praxis*. Muenchen: Franzis-Verlag.

Chayen, N. E., Snell, E. H., Helliwell, J. R. & Zagalsky, P. F. (1997). *J. Crystal Growth*, **171**, 219–225.

Chernov, A. A. (1984). *Modern Crystallography III: Growth of Crystals*, vol. 36 of *Springer Ser. Solid State*. Berlin: Springer.

Chernov, A. A. (1997). *J. Crystal Growth*, **174**, 254–261.

Chernov, A. A. & Komatsu, H. (1995). In *Science and Technology of Crystal Growth*, edited by J. P. van der Eerden & O. S. L. Bruinsma, pp. 329–353. Kluwer Ac. Pub.

Chernov, A. A. & Malkin, A. J. (1988). *J. Crystal Growth*, **92**, 432–444.

Durbin, S. & Carlson, W. (1992). *J. Crystal Growth*, **122**, 71–79.

Durbin, S., Carlson, W. & Saros, M. (1993). *J. Phys. D*, **26**, B128–B132.

Durbin, S. D. & Feher, G. (1986). *J. Crystal Growth*, **76**, 583–592.

García Ruiz, J. M. (1999). *J. Chem. Education*, **76**(4), 499–501.

García-Ruiz, J. M., Gavira, J. A., Otálora, F., Guasch, A. & Coll, M. (1998). *Mat. Res. Bull.* **33**(11), 1593–1598.

García-Ruiz, J. M., Novella, M. L. & Otálora, F. (1999). *J. Crystal Growth*, **196**, 703–710.

García Ruiz, J. M., Otálora, F., Novella, M. L., Gavira, J. A., Sauter, C. & Vidal, O. (2001). *J. Crystal Growth*, **232**, 149–155.

Gorti, S., Zuk, W. M., Konnert, J., Ward, K., Tanaka, T. & Yang, H. (2001). *J. Crystal Growth*, **232**, 256–261.

Hirano, E. & Ogawa, T. (1981). *J. Crystal Growth*, **51**, 113–118.

Hou, W. B., Kudryavtsev, A. B., Bray, T. L., DeLucas, L. J. & Wilson, W. W. (2001). *J. Crystal Growth*, **232**, 265–272.

Kam, Z., Shore, H. B. & Feher, G. (1978). *J. Mol. Biol.* **123**, 539–555.

Komatsu, H., Miyashita, S. & Suzuki, Y. (1993). *J. App. Phys.* **32**, L1855–L1857.

Konnert, J. H., D'Antonio, P. & Ward, K. B. (1994). *Acta Cryst.* D**50**, 603–613.

Kurihara, K., Miyashita, S., Sazaki, G., Nakada, T., Suzuki, Y. & Komatsu, H. (1996). *J. Crystal Growth*, **166**, 904–908.

Kuznetsov, Y., Malkin, A. J. & McPherson, A. (1999). *J. Crystal Growth*, **196**, 489–502.

Kuznetsov, Y. G., Malkin, A. J., Glantz, W. & McPherson, A. (1996*a*). *J. Crystal Growth*, **168**, 63–73.

Kuznetsov, Y. G., Malkin, A. J., Greenwood, A. & McPherson, A. (1995). *J. Struct. Biol.* **114**, 184–196.

Kuznetsov, Y. G., Malkin, A. J., Greenwood, A. & McPherson, A. (1996*b*). *J. Crystal Growth*, **166**, 913–918.

Kuznetsov, Y. G., Malkin, A. J. & McPherson, A. (2001). *J. Crystal Growth*, **232**, 114–118.

Land, T. A. & De Yoreo, J. J. (2000). *J. Crystal Growth*, **208**, 623–637.

Land, T. A., De Yoreo, J. J. & Lee, J. D. (1997). *Surf. Sci.* **384**, 136–155.

Land, T. A., Malkin, A. J., Kutznesov, Y. G., McPherson, A. & De Yoreo, J. J. (1996). *J. Crystal Growth*, **166**, 893–899.

Land, T. A., Malkin, A. J., Kuznetsov, Y. G., McPherson, A. & De Yoreo, J. J. (1995). *Phys. Rev. Lett.* **75**, 2774–2778.

Lautenschlager, P. (2002). APCF on ISS (Increment 3) data report. Astrium Doc. No. RP2220-0000 DO/22.

Li, H., Nadarajah, A. & Pusey, M. L. (1999). *Acta Cryst.* D**55**, 1036–1045.

Malkin, A. J., Kuznetsov, Y. G., Glantz, W. & McPherson, A. (1996). *J. Phys. Chem.* **100**(28), 11736–11743.

Malkin, A. J., Kuznetsov, Y. G. & McPherson, A. (1997). *Surf. Sci.* **393**, 95–107.

Malkin, A. J., Kuznetsov, Y. G. & McPherson, A. (1999). *J. Crystal Growth*, **196**, 471–488.

Malkin, A. J., Kuznetsov, Y. G. & McPherson, A. (2001). *J. Crystal Growth*, **232**, 173–183.

Maruyama, S., Yabana, J., Sumi, N., Komiya, A., Tsukamoto, K. & Shimizu, K. (1998). *J. Jpn. Soc. Microgravity Appl.* **15**(Supplement II), 571–576.

McPherson, A., Malkin, A. J. & Kuznetsov, Y. G. (1995). *Structure*, **3**(8), 759–768.

McPherson, A., Malkin, A. J., Kuznetsov, Y. G., Koszelak, S., Wells, M., Jenkins, G., Howard, J. & Lawson, G. (1999). *J. Crystal Growth*, **196**, 575–586.

Miers, H. A. (1904). *Phil. Trans.* A**202**, 492–515.

Miyashita, S., Komatsu, H., Suzuki, Y. & Nakada, T. (1994). *J. Crystal Growth*, **141**, 419–424.

Monaco, L. A. & Rosenberger, F. (1993). *J. Crystal Growth*, **129**, 465–484.

Muschol, M. & Rosenberger, F. (1996). *J. Crystal Growth*, **167**, 738–747.

Nakada, T., Sazaki, G., Miyashita, S., Durbin, S. D. & Komatsu, H. (1999). *J. Crystal Growth*, **196**, 503–510.

Onuma, K., Tsukamoto, K. & Nakadate, S. (1993). *J. Crystal Growth*, **129**, 706–718.

Otálora, F. & García-Ruiz, J. M. (1997). *J. Crystal Growth*, **182**, 141–154.

Otálora, F., Novella, M. L., Gavira, J. A., R.Thomas, B. & García-Ruiz, J. M. (2001). *Acta Cryst.* D**57**, 412–417.

Pusey, M., Witherow, W. & Naumann, R. (1988). *J. Crystal Growth*, **90**, 105–111.

Rashkovich, L. N. (1991). *KDP Family of Crystals.* New York: Adam-Hilger.

Robert, M. C., Vidal, O., García-Ruiz, J. M. & Otálora, F. (1999). In *Crystallization of Nucleic Acids and Proteins*, edited by A. Ducruix & R. Giegé, The Practical Approach Series, pp. 149–175. Oxford University Press.

Robinson, D. W. & Reid, G. T. (eds.) (1993). *Interferogram Analysis: Digital Fringe Pattern Measurement Techniques*. Institute of Physics Publishing.

Rong, L., Yamane, T. & Niimura, N. (2000). *J. Crystal Growth*, **217**, 161–169.

Rosenberger, F., Vekilov, P. G., Muschol, M. & Thomas, B. R. (1996). *J. Crystal Growth*, **168**, 1–27.

Savino, R. & Monti, R. (1996). *J. Crystal Growth*, **165**, 308–318.

Sazaki, G., Kurihara, K., Nakada, T., Miyashita, S. & Komatsu, H. (1996). *J. Crystal Growth*, **169**, 355–360.

Snell, E. H., Helliwell, J. R., Boggon, T. J., Lautenschlager, P. & Potthast, L. (1996). *Acta Cryst.* D**52**, 529–533.

Teng, H. H., Dove, P. M., Orme, C. & De Yoreo, J. J. (1998). *Science*, **282**, 724–727.

Thomas, B. R., Chernov, A. A., Vekilov, P. G. & Carter, D. C. (2000). *J. Crystal Growth*, **211**, 149–156.

Tsukamoto, K., yokoyama, E., Maruyama, S., Maiwa, K., Shimizu, K., Sekerka, R. F., Morita, T. S. & Yoda, S. (1998). *J. Jpn. Soc. Microgravity Appl.* **15**(1), 2–9.

Vekilov, P. & Rosenberger, F. (1998). *J. Crystal Growth*, **186**, 251–261.

Vekilov, P. G. (1993). *Prog. Crystal Growth and Charact.* **26**, 25–49.

Vekilov, P. G., Ataka, M. & Katsura, T. (1993). *J. Crystal Growth*, **130**, 317–320.

Vekilov, P. G., Monaco, L. A. & Rosenberger, F. (1995). *J. Crystal Growth*, **148**, 289–296.

Vekilov, P. G. & Rosenberger, F. (1996). *J. Crystal Growth*, **158**, 540–551.

Wiechmann, M., Enders, O., Zeilinger, C. & Kolb, H.-A. (2001). *Ultramicroscopy*, **86**, 159–166.

Yau, S. T., Thomas, B. R. & Vekilov, P. G. (2001). *J. Crystal Growth*, **232**, 188–194.



Received 18 April 2002 • Accepted 7 August 2002